RESEARCH ARTICLE

Ultra-Sensitive Visible-IR Range Fiber Based Plasmonic Sensor: A Finite-Element Analysis and Deep Learning Approach for RI Prediction

MOHAMMAD AL MAHFUZ[1,2], **(Member, IEEE), SUMAIYA AFROJ**[3], **AFIQUER RAHMAN**[4],
MD. AZAD HOSSAIN[2], **(Member, IEEE), MD. ANWAR HOSSAIN**[5], **(Senior Member, IEEE),**
AND MD SELIM HABIB[1], **(Senior Member, IEEE)**

[1]Department of Electrical Engineering and Computer Science, Florida Institute of Technology, Melbourne, FL 32901, USA
[2]Department of Electronics and Telecommunication Engineering, Chittagong University of Engineering and Technology, Chattogram 4349, Bangladesh
[3]Department of Biomedical Engineering, Bangladesh University of Engineering and Technology, Dhaka 1000, Bangladesh
[4]Department of Electronics and Telecommunication Engineering, Rajshahi University of Engineering and Technology, Rajshahi 6204, Bangladesh
[5]Department of Electrical and Electronic Engineering, Bangladesh University of Business and Technology, Dhaka 1216, Bangladesh

Corresponding author: Md Selim Habib (mhabib@fit.edu)

ABSTRACT In this paper, a relatively simple and ultra-sensitive Photonic crystal fiber (PCF) based surface plasmon resonance (SPR) sensor is proposed for detecting different analyte refractive indices (RIs) ranging from 1.33 to 1.43 over a wide range of wavelength spectrum spanning 0.55 μm to 3.50 μm. The comprehensive finite-element simulations indicate that it is possible to achieve remarkable sensing performances such as wavelength sensitivity (WS) and figure of merit (FOM) as high as 123,000 nm/RIU and 683 RIU^{-1}, respectively, and extremely low value of wavelength resolution (WR) about 8.13 $\times$ 10^{-7} RIU. A novel artificial neural network (ANN) model is proposed which helps to accurately predict the RIs by carefully examining the simulation data. The mean square error (MSE) and prediction accuracy (R^2) values for the ANN model are found about 0.0097 and 0.9987, respectively, indicating the high prediction capability of the proposed ANN model. Due to its exceptional sensitivity and precise detection capabilities, the proposed sensor has the potential to serve as a viable option for sensing analyte RI. Additionally, the sensor could be utilized for identifying cancerous cells and detecting urinary tract infections in humans.

INDEX TERMS Photonic crystal fiber, surface plasmon resonance, artificial neural network, sensor.

I. INTRODUCTION

Breakthrough research on surface plasmon resonance (SPR) technology has been widely demonstrated in various lab-on-chip devices, sensors, filters, and so on. Utilizing SPR in optical sensing proves advantageous due to its effectiveness, real-time detection capabilities, and user-friendly operations [1]. SPR technology holds promise for diverse applications such as food safety, security, medical testing, medical diagnostics, and biomolecular analyte detection [2]. Importantly, SPR sensors are appealing due to their reliability, efficiency, rapid response, effective light control capabilities, and label-free sensing, contributing to their widespread

The associate editor coordinating the review of this manuscript and approving it for publication was Mauro Fadda.

acceptance [3]. However, traditional SPR sensors relying on slot waveguide [4], fiber Bragg grating [5], and prism coupling [6], tend to be costly and bulky. Overcoming these limitations, optical fiber-based SPR sensors emerge as compact and cost-effective alternatives [7]. The success rate of bio-analyte sensing surpasses that of conventional methods, covering a range of applications including the detection of liquid analytes, gas, and cancer [8], [9], [10]. Plasmonic biosensors offering high-sensitivity refractive index detection have gained prominence. These encompass metal-based propagating eigenwaves RI sensors [11], nanoparticle-based localized surface plasmon resonance (LSPR) detectors [12], fano resonance RI sensors [13], and hybrid plasmonic-photonic sensors [14]. In contrast to conventional fiber optic sensors, in recent years there has been growing interest

in combining SPR technology with photonic crystal fiber (PCF) for sensing applications owing to the design flexibility, improved sensitivity, portability, lightweight construction, remote sensing capabilities, high birefringence properties, and single-mode guidance [15], [16]. The miniaturization of the device is possible for PCF sensors due to its physical dimensions [17] and guiding properties can also be controlled by modifying the geometric parameters [18]. In PCF-based plasmonic sensors, the coupling condition is greatly influenced by the surrounding environment, with the RI being a significant factor. Consequently, even slight alterations in the surrounding RI can potentially modify the resonance or coupling conditions. Therefore, detecting a shift in the resonance peak allows for the straightforward identification of an unknown analyte, as reported by Yang et al. [19].

In recent years, two types of PCF-based SPR sensing approaches have been studied namely internal sensing [20] and external sensing [21], [22], [23], [24]. In [20], the authors studied an internal plasmonic sensor with dual channels, involving a selective coating of metal around the air holes. This approach adds complexity to the device fabrication process, and the internal coating for both channels proves to be a time-consuming procedure. The performance of the sensor in [20] is comparatively low in which wavelength sensitivity (WS) and figure of merit (FOM) reached about 11,000 nm/RIU and 204 RIU^{-1}, respectively. In addition, the external sensing approach can potentially surpass the limitations of the internal sensing approach as the sensing medium and metal layer both are employed at the outer edge of the sensor and susceptible to the surrounding environment. A dual-core PCF based plasmonic external sensor was proposed by Mahfuz et al. [21], which shows WS of 28,000 nm/RIU and FOM is about 2800 RIU^{-1}. Here, the FOM is high, however, the WS is comparatively low. Recently, Srivastava and colleagues [22] numerically reported an external micro-channel D-shaped PCF-SPR sensor that explores WS of 67,000 nm/RIU and FOM of 279.16 RIU^{-1}. The micro-channel sensor provides relatively low FOM. Another intricate D-shaped SPR-PCF sensor was proposed in [23] in which WS of 216,000 nm/RIU and FOM of 1200 RIU^{-1} were obtained. These are outstanding results, however, the fabrication of D-shape structure is highly challenging and less practical since it requires precise surface polishing. Besides, Sharif and Pakarzadeh [24] proposed a circular PCF-SPR sensor for external sensing of samples which exhibits WS of 13,800 nm/RIU and FOM is about 470 RIU^{-1}. The sensing performance falls below the expected standard, and the range for sensing analyte refractive index is restricted, spanning from 1.29 to 1.34. The previous studies show either high WS and low FOM or vice-versa, along with fabrication challenges making them impractical for many real-world applications.

In our study, we propose a relatively simple and ultra-sensitive PCF-based SPR sensor considering external sensing technique which operates in a wide range of wavelengths for refractive index variation in the outer environment.
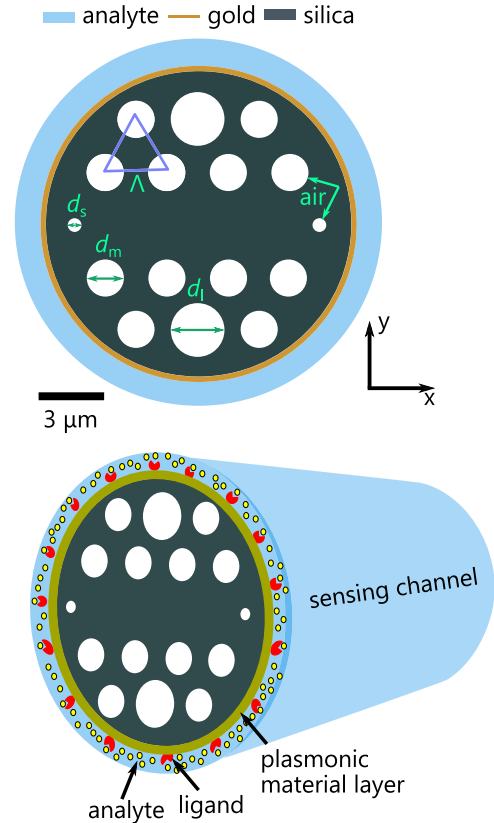

FIGURE 1. (Top) 2D geometry of the proposed sensor. Geometrical parameters are considered as below, two adjacent air-holes center to center distance, $\Lambda = 2.8$ μm, large air hole diameter, $d_l = 2.52$ μm, medium air hole diameter, $d_m = 1.68$ μm, small air hole diameter, $d_s = 0.56$ μm, gold layer thickness, $t_g = 35$ nm, and analyte layer thickness, $t_a = 1.4$ μm. (Bottom) 3D geometry of the proposed sensor.

The performance of the sensor is carried out in terms of WS, WR, and FOM. In addition, a deep learning model is suggested using the dataset obtained from simulation which can successfully predict the analyte refractive indices. The distinctive features of this study can be outlined as follows: (i) the fiber design is simple and flexible as compatible with various sample types including human urine and cancer cells, (ii) practical implementation of the senor is feasible as it utilizes only two hexagonal rings of air-holes employing external sensing approach, also the successful integration of FEM modeling with ANN architecture has real-time decision-making capability, (iii) broad RI sensing range covering the detection regime from visible to the infrared spectrum spanning 0.55 μm to 3.50 μm is suitable for diverse chemical, biomedical, and environmental monitoring, and (iv) remarkable sensing performances including low detection resolution is valuable for detecting trace amount of analytes in bio-sensing applications.

II. FIBER GEOMETRY AND THEORETICAL BACKGROUND
Fig. 1 (top) shows the two-dimensional view of the proposed PCF-based plasmonic RI sensor where the air-holes are arranged in two hexagonal rings on a silica (SiO$_2$) substrate.

Two air-holes from the inner ring are omitted in the horizontal direction and two air-holes from the outer ring in the same direction are scaled down so that the incident electromagnetic light can precisely excite the surface electrons. In the orthogonal direction, two air holes from the outer ring are scaled up which can assist to improve the performance of the sensor in the considered direction. In order to simplify the practical sensing approach, both the plasmonic material and sensing region are integrated into the outer surface of the fiber, serving as an external sensing layer. The fiber material employed is fused silica, and the dielectric constants can be derived from the Sellmeier equation, as outlined in [25].

Plasmonic materials play a vital role in the PCF-SPR sensor, which is responsible for generating surface plasmon polariton (SPP) waves in the fiber-dielectric interface. Considering the characteristics of broad shift of resonance valley, inertness, and longer stability in the environment, gold (Au) is used as plasmonic material and the dielectric function of gold is taken from the Drude-Lorentz Model [26]:

$$\epsilon_{Au} = \epsilon_\infty - \frac{\omega_D^2}{\omega(\omega + j\gamma_D)} - \frac{\Delta\epsilon\Omega_L^2}{(\omega^2 - \Omega_L^2) + j\Gamma_L\omega}, \quad (1)$$

where ε_{Au} = permittivity of Au and permittivity at high frequency $\varepsilon_\infty = 5.9673$. Other constants are taken from [26]. The sensing medium is placed at the external surface of the fiber and the sensor characteristic is changed with the changes of the outer environment. The target analyte can be detected with the functionalization of the Au film by varying the refractive index simultaneously. In 3D geometry (Fig. 1 (bottom)) the core region of silica is surrounded by capillary tube and maximum light will guide through the core region and enable substantial interaction between the core and metallic region to create SPP in the x-pol direction. An analyte flow channel is placed at the outer surface of the plasmonic material layer. When the analyte and ligand mutually interact with each other, the effective refractive index of the SPP-mode is expected to be varied resulting in a wavelength shift of the signal.

III. PHASE MATCHING PROPERTIES AND EM FIELD DISTRIBUTIONS

PCF-based SPR sensor working principle is based on guided electromagnetic evanescent field with appropriately designed core-cladding geometry. Free electrons stimulate from the metallic surface upon arrival of propagated light guided through the fiber core region. A surface plasmon wave (SPW) is generated when the event of frequency matching occurs. These SPWs are strongly sensitive to the surrounding RIs. Local RIs can be detected by properly observing the resonance or spectral wavelength variations [2]. Fig. 2 shows the phase-matching properties for local analyte RI of 1.39. It is evident from Fig. 2 that for the core-guided mode, the imaginary value of the effective mode index (violet) gradually increases, whereas the real value of the effective-mode index (red) gradually decreases with the increment of spectral
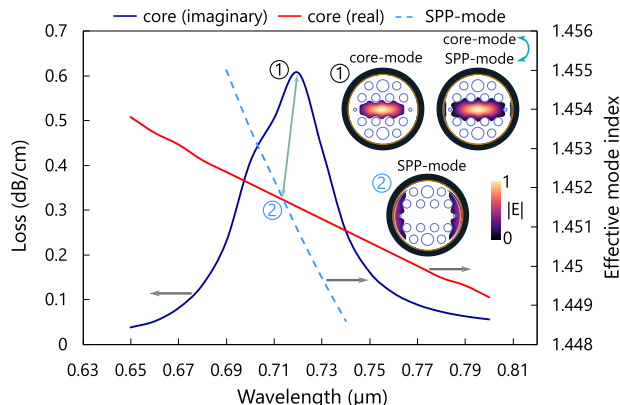

FIGURE 2. Phase matching properties for analyte RI of 1.39, where violet and red line show imaginary and real effective mode index for fundamental mode and broken light blue line indicates the SPP-mode, respectively. Inset figures represent the mode-field profiles for ① core-mode at wavelength 0.67 μm and coupling of core-mode and SPP-mode at 0.72 μm, and ② SPP-mode at 0.75 μm wavelength. The color bar shows the normalized mode-field profiles in a linear scale. The simulations are performed for $\Lambda = 2.8$ μm, $d_l = 2.52$ μm, $d_m = 1.68$ μm, $d_s = 0.56$ μm, $t_g = 35$ nm, and $t_a = 1.4$ μm in x–polarization direction.

wavelength. Besides, the real value of the effective-mode index (broken light blue) of SPP-mode gradually decreases and intersects with core-mode at a wavelength of 0.72 μm. This is the phase-matching point or resonance wavelength in which maximum energy transfers from the core-mode to the SPP-mode. The inset of Fig. 2:① shows the mode field distributions of core-mode and the coupling between core-mode and SPP-mode, whereas the inset of Fig. 2:② represents the SPP-mode for x–polarization.

IV. SIMULATION THEORY AND SENSOR PERFORMANCE ANALYSIS
The numerical simulations are performed through the finite-element method (FEM). To accurately model the fiber properties, a perfectly matched layer (PML) was incorporated outside the fiber domain, as outlined in [27], [28], [29], and [30]. Extremely fine mesh sizes are considered during simulations. In order to get a better sensing response, the fiber parameters are optimized by tuning a particular parameter, while other parameters remain unchanged. Due to showing the improved sensing response, the parameters are selected as $\Lambda = 2.8$ μm, $d_l = 2.52$ μm, $d_m = 1.68$ μm, $d_s = 0.56$ μm, t_g = 35 nm, and $t_a = 1.4$ μm. The proposed sensor performance is carried out using the confinement loss (CL) characteristics for various analytes. The CL was calculated using the well-known equation as in [31]. The sensitivity of the proposed plasmonic sensor is observed using the wavelength interrogation method and the wavelength sensitivity (WS) of the proposed plasmonic RI sensor is calculated using the following equation [32]:

$$S_\lambda = \frac{\Delta\lambda_{peak}}{\Delta n_a}(\text{nm/RIU}), \quad (2)$$

where $\Delta\lambda_{peak}$ and Δn_a indicate the wavelength shifting of the resonance peak and the RI variation of the two adjacent
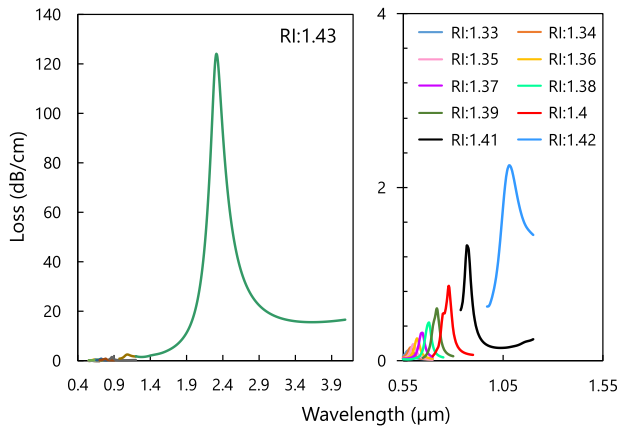
FIGURE 3. Confinement Loss curve for various analyte RIs from 1.33 to 1.43 in the wavelength between 0.5 to 4 μm (visible to IR range) using fiber geometrical parameters: Λ = 2.8 μm, d_l = 2.52 μm, d_m = 1.68 μm, d_s= 0.56 μm, t_g = 35 nm, and t_a = 1.4 μm in x−polarization direction.

TABLE 1. Details performance of the proposed RI sensor.

Analyte RI	Loss peak (dB/cm)	W_{peak} (μm)	S_{peak} (nm)	WS (nm/RIU)	FWHM (nm)	FOM (1/RIU)
1.33	0.11832	0.58	10	1000	50	20
1.34	0.15378	0.59	10	1000	40	25
1.35	0.19371	0.6	20	2000	40	50
1.36	0.25697	0.62	30	3000	40	75
1.37	0.32117	0.65	30	3000	40	75
1.38	0.43864	0.68	40	4000	40	100
1.39	0.60741	0.72	60	6000	40	150
1.4	0.86943	0.78	90	9000	50	180
1.41	1.3286	0.87	210	21000	50	420
1.42	2.2584	1.08	1230	123000	180	683
1.43	124.12	2.31	–	–	–	–

analytes, respectively. To observe the detection capability of the proposed sensor in the case of tiny analyte RIs variation, sensor resolution is a valuable metric which can be obtained from below equation [21]:

$$\text{WR} = \frac{\Delta n_a \times \Delta \lambda_{min}}{\Delta \lambda_{peak}} (\text{RIU}), \qquad (3)$$

where Δn_a, $\Delta \lambda_{peak}$, and $\Delta \lambda_{min}$ indicate the variation of two adjacent tiny RIs, loss peak shifting and minimum resolution of the detector, respectively. During the measurement of sensor resolution external perturbation and instrumental noise are not considered [21]. In determining the quantitative performance of the sensor, it is crucial to compute the figure of merit (FOM), as expressed in the following equation [33]:

$$\text{FOM} = \frac{\text{Wavelegth sensitivity}}{\text{FWHM}} (\text{RIU}^{-1}), \qquad (4)$$

where FWHM stands for full width at half maximum, and high FOM indicates the better detection limit of the sensor.

In this study, the observation of the sensor's performance focuses solely on the x−polarization mode due to the stronger coupling between core and SPP-mode. Fig. 3 illustrates the CL spectra while varying the sample refractive indices within the range of 1.33 to 1.43. According to Fig. 3, CL curves growing and red-shifted simultaneously with the increasing of analyte RIs. This phenomenon occurred due to the RIs contrast reduction from core-mode to SPP-mode, hence, evanescent electromagnetic light coupling through the metal-dielectric interface efficiently increased and loss peak experienced an upward trend. It can be seen from Fig. 3 that the lowest loss peak value of 0.11832 dB/cm appeared for RI of 1.33 at the wavelength of 0.58 μm and it reached the highest peak value of 124.12 dB/cm at wavelength of 2.31 μm for RI of 1.43. The other CL peak values are found 0.15378, 0.19371, 0.25697, 0.32117, 0.43864, 0.60741, 0.86943, 1.3286, and 2.2584 dB/cm, respectively, for analyte RIs from 1.34 to 1.42 in the wavelength range between 0.59 and

1.08 μm. Using Eq. (2) the minimum wavelength sensitivity (WS) is obtained about 1000 nm/RIU for analyte RI of 1.33 and the maximum WS reached about 123,000 nm/RIU for sample RI of 1.42. Besides, the minimum wavelength resolution is measured about 8.13×10^{-7} RIU for analyte RI of 1.42, which indicates that the proposed sensor is capable of detecting very tiny changes of analyte RIs even in the order of 10^{-7} scale and maximum FOM obtained about 683 RIU^{-1} for analyte RI of 1.42 using Eqs. (3) and (4), respectively. The performance of the proposed sensor is briefly tabulated in Table 1. In this study, the detectable RI range is 1.33 − 1.43 which span is significant for various cell biology research and disease diagnoses [34]. Fig. 4 illustrates that the proposed sensor can potentially detect the various cancer-affected cells by observing the resonance valley shift from the normal cell. The CL peaks appeared at 0.62, 0.64, 0.66, 0.68, 0.7, and 0.71 μm wavelength for normal cells of basal (30-70%), HeLa (30-70%), Jurkat (30-70%), PC12 (30-70%), MDA-MB-231 (30-70%), and MCF 7 (30-70%), respectively. However, when the cells are affected by skin (80%), cervical (80%), blood (80%), adrenal glands (80%), and breast (80%) cancers then the zenith peaks are moved to the longer wavelength which are found at 0.68, 0.73, 0.72, 0.75, 0.78, and 0.79 μm with showing WS of 6000, 7000, 6000, 7000, 8000, and 8000 nm/RIU, respectively. Importantly, the sensor exhibits low loss characteristics (below 1 dB/cm), making it an excellent choice for detecting various cancerous cells in the visible regime. Here, the relevant RIs values are taken from Ref. [35].

For the further applications of the sensor, in this work, we have figured out the sensing response in terms of human urine disease detection as depicted in Fig. 5. From Fig. 5, it is noticeable that the resonance valley is changed from its normal position when it is affected by disease. For normal urine (RI = 1.3464) the CL peak is found at 0.595 μm wavelength and after being affected by disease it is shifted to the shorter wavelength at 0.585 and 0.59 μm for acute and moderate disease showing WS about 1000 and 500 nm/RIU, respectively. In the case of above normal, it is shifted to the longer wavelength of 0.6 μm, hence, the WS is 500 nm/RIU. In this specific detection study, the loss peak remains below 0.2 dB/cm which is comparatively lower than the [39],
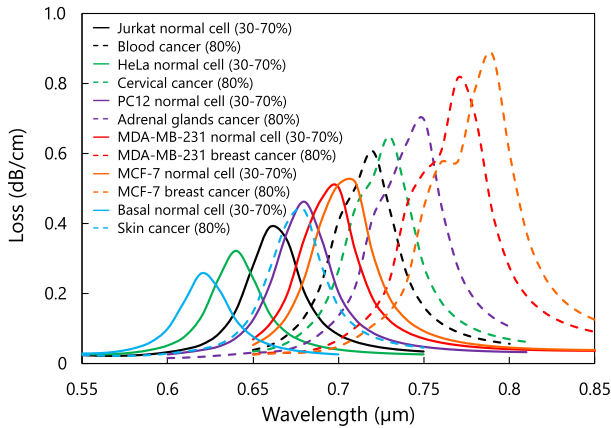
FIGURE 4. Resonance peak shifting for six different biological cells and the dotted curves indicate the cancer-affected cell whereas the smooth curves represent normal cells.
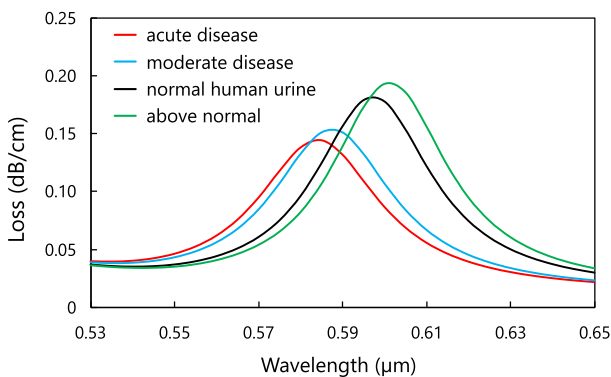

FIGURE 5. Observation of resonance peak shifting due to human urine infections. The RIs of normal human urine, moderate disease, acute disease, and above normal are 1.3464, 1.3396, 1.337, and 1.3489, respectively.

TABLE 2. Performance comparison with the reported PCF-based SPR sensor.

Refs.	Sensing type (Fiber shape)	WS (nm/RIU)	WR (RIU)	FOM (1/RIU)	Detection range
[17]	External (Spiral PCF)	4600	2.17×10^{-5}	–	1.33–1.38
[20]	Internal (Coated PCF)	11000	9.09×10^{-5}	204	1.33–1.41
[23]	External (D-shape PCF)	216,000	4.63×10^{-7}	1200	1.33–1.42
[24]	External (Circular PCF)	13800	7.24×10^{-6}	470	1.29–1.34
[26]	External (Circular PCF)	30000	3.33×10^{-6}	508	1.33–1.39
[32]	External (Dual D-shape PCF)	24300	4.12×10^{-6}	120	1.10–1.45
[36]	External (Multi-channel PCF)	45800	–	635	1.36–1.42
[37]	Micro-channel (D-shape PCF)	20000	5×10^{-6}	–	1.18–1.36
[38]	Internal (Coated PCF)	11000	9.1×10^{-6}	407	1.33–1.42
Proposed	External (Circular PCF)	123,000	8.13×10^{-7}	683	1.33–1.43

hence it can be a good candidate for biochemical sensing applications. For this analysis, the RIs values are taken from the following [40]. To validate the numerical results

of the proposed sensor, the performance is benchmarked with the published literature and tabulated in Table 2. The schematic view of the experimental consideration for this work can be carried out as outlined in [16] and [21]. The proposed two ring hexagonal lattice PCF based SPR sensor can be practically implemented with the capillary stacking or stack-and-draw fabrication technique [36] where the air-holes can be realized with employing thicker wall capillaries, and the missing air-holes can be realized with using solid-rods. There are several methods exists to deposit the outer plasmonic material (gold) such as wet-chemistry deposition and thermal evaporation [41]. However, the major limitation of these methods is excessive surface roughness during deposition. On that perspective, to minimize the surface roughness and to have a uniformly nano-layer coating, chemical vapor deposition (CVD) and atomic layer deposition (ALD) methods are highly accepted [21], [42], [43]. In this study, fused silica is used as the background material, which has an ultra-low thermal sensitivity. The RIs variation with temperature for fused silica is as low as $1.28 \times 10^{-5}/^o$c. Therefore, the temperature effect can be ignored in normal environments without severe temperature variations.

V. ANN MODEL FOR PREDICTION OF RIS WITH DATA OBTAINED FROM THE SENSOR

This section introduces an artificial neural network (ANN) model integrated at the termination of the spectrum analyzer within the practical configuration of the sensor. The primary objective is to enhance the precision of the bio-analyte RI prediction technique subsequent to the acquisition of resonance wavelength (λ_r) and peak confinement loss. The ANN structure is displayed in Fig. 6, configured to take (λ_r) and loss as inputs (i) and yield the corresponding RI as output (o). The distinct advantage of employing this model lies in its ability to significantly reduce human intervention in RI detection. The dataset for model training encompasses a spectrum of RI values ranging from 1.33 to 1.43, strategically chosen to reflect diverse bio-samples. For each RI, data points consist of resonance wavelength, four neighboring wavelengths, and corresponding confinement losses, ensuring resilience against fabrication errors leading to deviations in resonance wavelength. The input features and the output target are extracted, and in MaxScaler [44] is applied to normalize both input and output variables. The dataset is partitioned into a 7:3 ratio for training and validation purposes. The neural network model is constructed using the Sequential API from Keras [45]. It consists of an input layer with 2 nodes corresponding to the number of features, followed by three dense layers with 512, 32, and 160 nodes, respectively, and varying activation functions (swish [46] and relu [47]). Each hidden layer in a neural network uses activation functions to conduct a weighted sum or nonlinear processing on the values received from the prior layer. The output layer receives the updated value from the
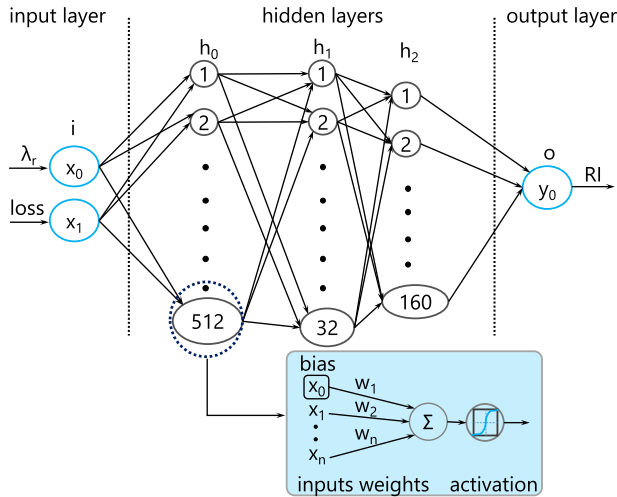
FIGURE 6. Structure of the neural network consisting of 3 hidden layers with different numbers of neurons in each layer. The input layer consists of two nodes: resonance wavelength (λ_r) and confinement loss. The output layer has one node: refractive index (RI). The mechanism of the activation function at each node is depicted in the smaller block.

TABLE 3. Inputs and predicted output from the neural network and their corresponding absolute percentage error.

Neural network input		Predicted	Actual	
RW (µm)	CL (dB/cm)	RI	RI	|Error (%)|
0.580	0.11832	1.330000	1.3300	0
0.585	0.14449	1.337010	1.3370 (Acute disease)	$7.48 \cdot 10^{-4}$
0.595	0.17909	1.346900	1.3464 (Normal urine)	$3.70 \cdot 10^{-2}$
0.660	0.38897	1.375954	1.3760 (Normal cell jurkat)	$3.34 \cdot 10^{-3}$
0.750	0.69604	1.394826	1.3950 (Adrenal glands cancer)	$1.24 \cdot 10^{-2}$
0.780	0.70629	1.399046	1.3990 (MDA-MB-231)	$3.28 \cdot 10^{-3}$
2.310	124.120	1.430759	1.4300	$5.30 \cdot 10^{-2}$

FIGURE 7. MSE during the training process against each epoch. The loss function stabilizes reaching the value of 0.0097 at around 80 epochs. The violet dot represents the training loss and the validation loss is depicted by green dot.

FIGURE 8. Actual RI vs predicted RI demonstrating the predictability of the model. Predicted RIs are marked with black markers and the blue line represents the actual RI. The predicted RIs do not deviate much from the actual RI for inputs consisting of resonance wavelength and magnitude of confinement loss in the training range.

last concealed layer. Stochastic Gradient Descent (SGD), as outlined by Xu et al. [48], is critical in maximizing all parameters via the connections made in the feed-forward process:

$$\text{weight}' = \text{weight} - \text{lr} \cdot \frac{\partial \text{loss}(Y, \hat{Y})}{\partial \text{weight}}. \tag{5}$$

$$\text{bias}' = \text{bias} - \text{lr} \cdot \frac{\partial \text{loss}(Y, \hat{Y})}{\partial \text{bias}}. \tag{6}$$

In this context, the learning rate (lr) is an important component. Neurons undergo nonlinear transformations via the activation function, as described by Leshno et al. [49]. Because of this property, ANNs can approximate any desired function. In our method, we chose a very complex neural network rather than the traditional ANN topologies commonly used for regression problems. The complexity was added to improve prediction accuracy.

Notably, the last layer is made up of a single node with a linear activation function, making it an excellent choice for regression-oriented applications. All the hyperparameters
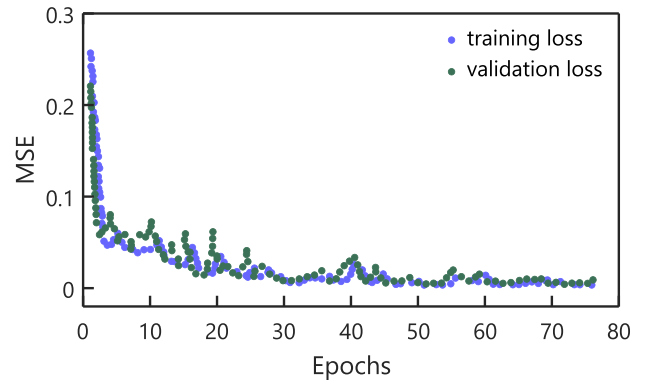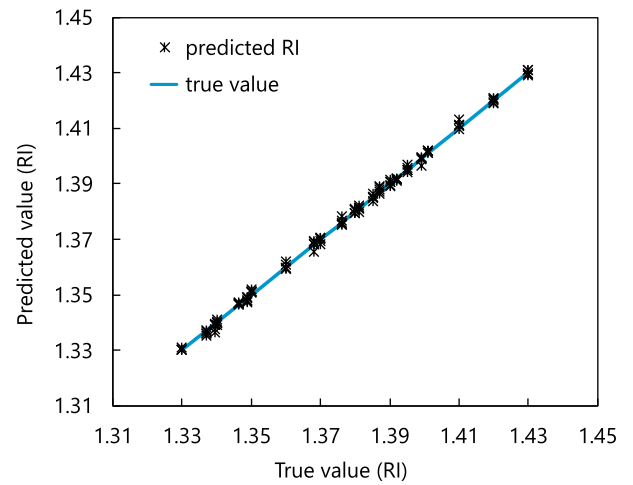
for the ANN are tuned based on trial and error method. The model is compiled using the Nadam [50] optimizer with a specified learning rate and Mean squared error (MSE) as the loss function. As mentioned in [51], the goal of this adjustment procedure is to reduce the MSE between the expected and actual output values. Formulating a loss function specifically for the regression problem is as follows:

$$\text{MSE} = \frac{1}{n} \sum_{i=0}^{n} (y_i - \hat{y}_i)^2, \tag{7}$$

where n is the number of data points and y_i and $\hat{y}_i$ is the actual and predicted result respectively. Early stopping is implemented with a patience of 100 epochs to prevent over-fitting. Training and validation loss over epochs, providing a visual representation of the model's learning progress is evident in Fig. 7. The MSE for the test dataset is obtained to be 0.0097. Fig. 8 presents the predicted RIs compared to the actual values, underscoring the regression model's accuracy. The R^2 value for the predicted result obtained is 0.9987.

Some of the prediction results and their corresponding absolute percentage error (APE) are tabulated in Table 3. The testing points used were completely new to the neural network and were not part of the training datasets. Because the network is tested on data not encountered during the learning phase, this method ensures an unbiased evaluation of its prediction skills. Since our study mainly focused on finite-element modeling, we have introduced a novel ANN model to accurately predict the RIs of various analytes. According to Table 3, the ANN model demonstrates a significant potential for predicting the RIs of different cancerous cells. This novel approach paves the way for detecting cancerous cells precisely with high sensitivity, even in the absence of experimental validations.

VI. CONCLUSION

In this study, we proposed, simulated, and analyzed an ultra-sensitive PCF-based SPR RI sensor that operates across the visible to infrared spectrum, ranging from 0.55 μm to 3.50 μm. The sensor achieved outstanding performance metrics, with a maximum wavelength sensitivity of 123,000 nm/RIU, a minimum wavelength resolution of 8.13×10^{-7} RIU, and a figure of merit (FOM) of 683 RIU^{-1}. It effectively covers a RI range from 1.33 to 1.43, allowing for the detection of tiny changes in sample analyte RI on the order of 10^{-7}. This capability enables the sensor to identify a wide array of substances, from various cancer cells to biomolecules and biochemicals, making it a versatile tool for optical sensing applications. Furthermore, the integration of a novel deep learning technique improved the sensor's accuracy and reduced losses, paving the way for innovative solutions in a range of applications, including lab-on-chip technologies. This study demonstrates the sensor's potential to significantly impact the field of optical sensing due to its high sensitivity and broad detection range.

REFERENCES

[1] C. M. Das, F. Yang, Z. Yang, X. Liu, Q. T. Hoang, Z. Xu, S. Neermunda, K. V. Kong, H. Ho, L. A. Ju, J. Xiong, and K. Yong, "Computational modeling for intelligent surface plasmon resonance sensor design and experimental schemes for real-time plasmonic biosensing: A review," *Adv. Theory Simulations*, vol. 6, no. 9, Sep. 2023, Art. no. 2200886.

[2] A. A. Rifat, R. Ahmed, A. K. Yetisen, H. Butt, A. Sabouri, G. A. Mahdiraji, S. H. Yun, and F. R. M. Adikan, "Photonic crystal fiber based plasmonic sensors," *Sens. Actuators B, Chem.*, vol. 243, pp. 311–325, May 2017.

[3] S. Singh, B. Chaudhary, A. Upadhyay, D. Sharma, N. Ayyanar, and S. A. Taya, "A review on various sensing prospects of SPR based photonic crystal fibers," *Photon. Nanostruct. Fundam. Appl.*, vol. 54, May 2023, Art. no. 101119.

[4] V. Laxmi, A. Parveen, D. Tyagi, L. Singh, and Z. Ouyang, "Nanophotonic modulator based on silicon-ITO heterojunction and slot waveguide with 2D-graphene sheet," *J. Opt.*, vol. 52, no. 3, pp. 984–994, Sep. 2023.

[5] M. Mishra and P. K. Sahu, "Fiber Bragg gratings in healthcare applications: A review," *IETE Tech. Rev.*, vol. 40, no. 2, pp. 202–219, Mar. 2023.

[6] O. Bolduc, L. Live, and J. Masson, "High-resolution surface plasmon resonance sensors based on a dove prism," *Talanta*, vol. 77, no. 5, pp. 1680–1687, Mar. 2009.

[7] J. Jing, K. Liu, J. Jiang, T. Xu, S. Wang, J. Ma, Z. Zhang, W. Zhang, and T. Liu, "Performance improvement approaches for optical fiber SPR sensors and their sensing applications," *Photon. Res.*, vol. 10, no. 1, pp. 126–147, 2022.

[8] F. Mumtaz, G. Yaseen, M. Roman, L. G. Abbas, M. A. Ashraf, M. A. Fiaz, and Y. Dai, "Numerical analysis of the highly non-linear and ultra-sensitive modified core of a photonic crystal fiber sensor for detection of liquid analytes," *J. Opt. Soc. Amer. B, Opt. Phys.*, vol. 40, no. 1, pp. 142–150, 2023.

[9] Y. Liu, Y. Chen, C. Li, and X. Yang, "Copper-multiwalled carbon nanotubes decorated fiber-optic surface plasmon resonance sensor for detection of trace hydrogen sulfide gas," *Opt. Fiber Technol.*, vol. 76, Mar. 2023, Art. no. 103221.

[10] B. Kaur, S. Kumar, and B. K. Kaushik, "Recent advancements in optical biosensors for cancer detection," *Biosensors Bioelectron.*, vol. 197, Feb. 2022, Art. no. 113805.

[11] M. D. Baiad and R. Kashyap, "Concatenation of surface plasmon resonance sensors in a single optical fiber using tilted fiber Bragg gratings," *Opt. Lett.*, vol. 40, no. 1, pp. 115–118, 2015.

[12] Q. Li, X. Zhuo, S. Li, Q. Ruan, Q. Xu, and J. Wang, "Production of monodisperse gold nanobipyramids with number percentages approaching 100% and evaluation of their plasmonic properties," *Adv. Opt. Mater.*, vol. 3, no. 6, pp. 801–812, Jun. 2015.

[13] Y. Bao, Z. Hu, Z. Li, X. Zhu, and Z. Fang, "Magnetic plasmonic Fano resonance at optical frequency," *Small*, vol. 11, no. 18, pp. 2177–2181, May 2015.

[14] M. D. Baaske, M. R. Foreman, and F. Vollmer, "Single-molecule nucleic acid interactions monitored on a label-free microcavity biosensor platform," *Nature Nanotechnol.*, vol. 9, no. 11, pp. 933–939, Nov. 2014.

[15] Y. Zhao, X.-G. Hu, S. Hu, and Y. Peng, "Applications of fiber-optic biochemical sensor in microfluidic chips: A review," *Biosensors Bioelectron.*, vol. 166, Oct. 2020, Art. no. 112447.

[16] M. A. Mahfuz, M. R. Hasan, M. R. Momota, A. Masud, and S. Akter, "Asymmetrical photonic crystal fiber based plasmonic sensor using the lower birefringence peak method," *OSA Continuum*, vol. 2, no. 5, pp. 1713–1725, 2019.

[17] Md. R. Hasan, S. Akter, A. A. Rifat, S. Rana, K. Ahmed, R. Ahmed, H. Subbaraman, and D. Abbott, "Spiral photonic crystal fiber-based dual-polarized surface plasmon resonance biosensor," *IEEE Sensors J.*, vol. 18, no. 1, pp. 133–140, Jan. 2018.

[18] M. A. Mahfuz, M. A. Mollah, M. R. Momota, A. K. Paul, A. Masud, S. Akter, and M. R. Hasan, "Highly sensitive photonic crystal fiber plasmonic biosensor: Design and analysis," *Opt. Mater.*, vol. 90, pp. 315–321, Apr. 2019.

[19] Y. Yang, S. Bandyopadhyay, L. Shao, J. Jiang, Z. Peng, S. Liu, J. Hu, P. P. Shum, J. Hu, and X. Zhang, "Anomalous sensitivity enhancement of D-shaped fiber-based sandwiched structure optofluidic sensor," *IEEE Access*, vol. 8, pp. 105207–105216, 2020.

[20] M. F. Azman, M. Mashrafi, F. Haider, R. Ahmed, R. A. Aoni, M. Junayed, W. W. Ru, G. A. Mahdiraji, and F. R. M. Adikan, "Polarization selective PCF-based plasmonic biosensor for multi-analyte detection," *Plasmonics*, pp. 1–10, 2024.

[21] M. A. Mahfuz, M. A. Hossain, E. Haque, N. H. Hai, Y. Namihira, and F. Ahmed, "Dual-core photonic crystal fiber-based plasmonic RI sensor in the visible to near-IR operating band," *IEEE Sensors J.*, vol. 20, no. 14, pp. 7692–7700, Jul. 2020.

[22] R. Srivastava, Y. K. Prajapati, S. Pal, and S. Kumar, "Micro-channel plasmon sensor based on a D-shaped photonic crystal fiber for malaria diagnosis with improved performance," *IEEE Sensors J.*, vol. 22, no. 15, pp. 14834–14841, Aug. 2022.

[23] E. Haque, A. A. Noman, M. A. Hossain, N. H. Hai, Y. Namihira, and F. Ahmed, "Highly sensitive D-shaped plasmonic refractive index sensor for a broad range of refractive index detection," *IEEE Photon. J.*, vol. 13, no. 1, pp. 1–11, Feb. 2021.

[24] V. Sharif and H. Pakarzadeh, "High-performance surface plasmon resonance fiber sensor based on cylindrical vector modes," *Sci. Rep.*, vol. 13, no. 1, p. 4563, Mar. 2023.

[25] C. Z. Tan, "Determination of refractive index of silica glass for infrared wavelengths by IR spectroscopy," *J. Non-Crystalline Solids*, vol. 223, nos. 1–2, pp. 158–163, Jan. 1998.

[26] F. Haider, R. A. Aoni, R. Ahmed, M. S. Islam, and A. E. Miroshnichenko, "Propagation controlled photonic crystal fiber-based plasmonic sensor via scaled-down approach," *IEEE Sensors J.*, vol. 19, no. 3, pp. 962–969, Feb. 2019.

[27] M. S. Habib, M. S. Habib, S. M. A. Razzak, and M. A. Hossain, "Proposal for highly birefringent broadband dispersion compensating octagonal photonic crystal fiber," *Opt. Fiber Technol.*, vol. 19, no. 5, pp. 461–467, Oct. 2013.

[28] M. S. Habib, O. Bang, and M. Bache, "Low-loss hollow-core silica fibers with adjacent nested anti-resonant tubes," *Opt. Exp.*, vol. 23, no. 13, pp. 17394–17406, 2015.

[29] M. S. Habib, J. E. Antonio-Lopez, C. Markos, A. Schülzgen, and R. Amezcua-Correa, "Single-mode, low loss hollow-core anti-resonant fiber designs," *Opt. Exp.*, vol. 27, no. 4, pp. 3824–3836, 2019.

[30] M. A. Cooper, J. Wahlen, S. Yerolatsitis, D. Cruz-Delgado, D. Parra, B. Tanner, P. Ahmadi, O. Jones, M. S. Habib, I. Divliansky, J. E. Antonio-Lopez, A. Schülzgen, and R. A. Correa, "2.2 kW single-mode narrow-linewidth laser delivery through a hollow-core fiber," *Optica*, vol. 10, no. 10, pp. 1253–1259, 2023.

[31] M. I. Hasan, M. S. Habib, M. S. Habib, and S. M. A. Razzak, "Highly nonlinear and highly birefringent dispersion compensating photonic crystal fiber," *Opt. Fiber Technol.*, vol. 20, no. 1, pp. 32–38, Jan. 2014.

[32] N. Hussain, M. R. Masuk, M. F. Hossain, and A. Z. Kouzani, "Dual core photonic crystal fiber based plasmonic refractive index sensor with ultra-wide detection range," *Opt. Exp.*, vol. 31, no. 16, pp. 26910–26922, 2023.

[33] Y. Feng, W. Zhang, T. Xu, L. Huang, C. Liu, and T. Shen, "Design and research of a dual-parameter photonic crystal fiber sensor," *J. Opt. Soc. Amer. B, Opt. Phys.*, vol. 40, no. 5, pp. 1267–1276, 2023.

[34] P. Y. Liu, L. K. Chin, W. Ser, H. F. Chen, C.-M. Hsieh, C.-H. Lee, K.-B. Sung, T. C. Ayi, P. H. Yap, B. Liedberg, K. Wang, T. Bourouina, and Y. Leprince-Wang, "Cell refractive index for cell biology and disease diagnosis: Past, present and future," *Lab Chip*, vol. 16, no. 4, pp. 634–644, 2016.

[35] M. A. Jabin, K. Ahmed, M. J. Rana, B. K. Paul, M. Islam, D. Vigneswaran, and M. S. Uddin, "Surface plasmon resonance based titanium coated biosensor for cancer cell detection," *IEEE Photon. J.*, vol. 11, no. 4, pp. 1–10, Aug. 2019.

[36] K. M. M. Rahman, M. S. Alam, and M. A. Islam, "Highly sensitive surface plasmon resonance refractive index multi-channel sensor for multi-analyte sensing," *IEEE Sensors J.*, vol. 21, no. 24, pp. 27422–27432, Dec. 2021.

[37] E. Haque, M. A. Hossain, F. Ahmed, and Y. Namihira, "Surface plasmon resonance sensor based on modified *D*-shaped photonic crystal fiber for wider range of refractive index detection," *IEEE Sensors J.*, vol. 18, no. 20, pp. 8287–8293, Oct. 2018.

[38] A. A. Rifat, F. Haider, R. Ahmed, G. A. Mahdiraji, F. R. M. Adikan, and A. E. Miroshnichenko, "Highly sensitive selectively coated photonic crystal fiber-based plasmonic sensor," *Opt. Lett.*, vol. 43, no. 4, pp. 891–894, 2018.

[39] P. Manickam and R. Senthil, "Numerical demonstration of photonic quasi-crystal fiber–surface plasmonic resonance urinary methanol sensor," *Plasmonics*, vol. 18, no. 2, pp. 511–519, Apr. 2023.

[40] A. V. Wolf, *Aqueous Solutions and Body Fluids: Their Concentrative Properties and Conversion Tables*. New York, NY, USA: Harper & Row, 1966.

[41] A. A. Rifat, M. R. Hasan, R. Ahmed, and H. Butt, "Photonic crystal fiber-based plasmonic biosensor with external sensing approach," *J. Nanophotonics*, vol. 12, no. 1, Jun. 2017, Art. no. 012503.

[42] P. O. Oviroh, R. Akbarzadeh, D. Pan, R. A. M. Coetzee, and T.-C. Jen, "New development of atomic layer deposition: Processes, methods and applications," *Sci. Technol. Adv. Mater.*, vol. 20, no. 1, pp. 465–496, Dec. 2019.

[43] K. K. Gleason, *CVD Polymers: Fabrication of Organic Surfaces and Devices*. Hoboken, NJ, USA: Wiley, 2015.

[44] P. Misra and A. S. Yadav, "Impact of preprocessing methods on healthcare predictions," in *Proc. 2nd Int. Conf. Adv. Comput. Softw. Eng. (ICACSE)*, 2019, pp. 144–150.

[45] N. Ketkar, "Introduction to Keras," in *Deep Learning With Python*. Cham, Switzerland: Springer, 2017, pp. 97–111.

[46] M. Gustineli, "A survey on recently proposed activation functions for deep learning," 2022, *arXiv:2204.02921*.

[47] A. Fred Agarap, "Deep learning using rectified linear units (ReLU)," 2018, *arXiv:1803.08375*.

[48] Y. Xu, X. Zhang, Y. Fu, and Y. Liu, "Interfacing photonics with artificial intelligence: An innovative design strategy for photonic structures and devices based on artificial neural networks," *Photon. Res.*, vol. 9, no. 4, pp. B135–B152, 2021.

[49] M. Leshno, V. Y. Lin, A. Pinkus, and S. Schocken, "Multilayer feedforward networks with a nonpolynomial activation function can approximate any function," *Neural Netw.*, vol. 6, no. 6, pp. 861–867, Jan. 1993.

[50] J. Wang and Z. Cao, "Chinese text sentiment analysis using LSTM network based on L2 and Nadam," in *Proc. IEEE 17th Int. Conf. Commun. Technol. (ICCT)*, Oct. 2017, pp. 1891–1895.

[51] O. Bunke and B. Droge, "Estimators of the mean squared error of prediction in linear regression," *Technometrics*, vol. 26, no. 2, pp. 145–155, May 1984.

MOHAMMAD AL MAHFUZ (Member, IEEE) received the Bachelor of Science degree in electronics and telecommunication engineering from Rajshahi University of Engineering and Technology, in 2018, Bangladesh. He is currently pursuing the Ph.D. degree with the Department of Electrical Engineering and Computer Science, Florida Institute of Technology, USA. His research interests include hollow core fiber, photonic crystal fiber, photonic sensor, and metamaterial.

SUMAIYA AFROJ received the Bachelor of Science degree in biomedical engineering from Khulna University of Engineering and Technology, Bangladesh. She is currently pursuing the Master of Science degree in biomedical engineering with Bangladesh University of Engineering and Technology, Bangladesh. Her research interests include biosensors, biophotonics, breast cancer, and biomaterials.

AFIQUER RAHMAN is currently pursuing the bachelor's degree in electronics and telecommunication engineering with Rajshahi University of Engineering and Technology. His research interest includes combining machine learning with optical sensors to improve sensing technologies. He is dedicated to pushing the boundaries and contributing valuable insights to bridge traditional methods with modern applications.

MD. AZAD HOSSAIN (Member, IEEE) received the B.Sc. degree from the Department of Electrical and Electronic Engineering, Rajshahi University of Engineering and Technology (RUET), in 2004, and the M.Sc. and Ph.D. degrees from Saga University, Saga, Japan, in 2010 and 2013, respectively. He is currently a Professor with the Department of Electronics and Telecommunication Engineering, Chittagong University of Engineering and Technology (CUET). His research interests include antenna for polarization switching and detection, antenna for biomedical applications, brain stimulation, RF energy harvesting, 5G antenna, and MIMO antenna design.

MD. ANWAR HOSSAIN (Senior Member, IEEE) received the B.Sc. (Engineering) degree in electrical and electronic engineering from Rajshahi University of Engineering and Technology, Rajshahi, Bangladesh, in 2001, the M.E. degree in information and communication technology from Asian Institute of Technology, Pathum Thani, Thailand, in 2006, and the Ph.D. degree in electronics and information engineering under interdisciplinary intelligent systems engineering from the University of the Ryukyus, Nishihara, Japan, in 2013. He is currently a Professor with the Electrical and Electronic Engineering Department, Bangladesh University of Business and Technology (BUBT), Dhaka, Bangladesh. He is also doing research with the Electrical and Electronic Engineering Department, Independent University, Bangladesh (IUB); the School of Electronics and Telecommunications, Hanoi University of Science and Technology, Vietnam; and the University of the Ryukyus, Japan. His research interests include photonic sensors, biophotonics, photonic crystals fibers, optoelectronic devices and systems, antenna array signal processing (beamforming), CDMA, optical CDMA, and OFDM. He received the Postdoctoral Fellowship from Japan Society for the Promotion of Science in 2015.

MD SELIM HABIB (Senior Member, IEEE) received the Ph.D. degree in electrical and photonics engineering from the Technical University of Denmark (DTU), in 2017.

Following the completion of the Ph.D. degree, he joined the Fibers Sensors and Supercontinuum Group, Department of Electrical and Photonics Engineering, DTU, as a Postdoctoral Researcher. After concluding his Postdoctoral Fellowship with DTU, he was a Postdoctoral Research Associate with the CREOL, College of Optics and Photonics, University of Central Florida, USA, from 2017 to 2019. From 2019 to 2023, he held the position of an Assistant Professor of electrical and computer engineering with Florida Polytechnic University, USA. He is currently an Assistant Professor of electrical engineering with Florida Institute of Technology. He has published more than 50 articles in refereed journals. His research interests include computational electromagnetics, emerging optical fiber design, fabrication, characterization, and ultrafast nonlinear optics. He is a Senior Member of Optica (formerly OSA) and the Executive Officer of the OSA Fiber modeling and Fabrication Group. He received the University Gold Medal Award from Rajshahi University of Engineering and Technology in 2014. He is an Associate Editor of IEEE JOURNAL OF LIGHTWAVE TECHNOLOGY and the Feature Editor of *Applied Optics*.

• • •